CHAPTER 8

Photodegradation of Rhodamine B using Ag-doped $Bi_2WO_6/Bi_{14}W_2O_{27}$ composite film fabricated by a chemical deposition method

Chapter eight is mentioned the characterization and photocatalytic activity of Ag-doped $Bi_2WO_6/Bi_{14}W_2O_{27}$ composite film, which fabricated by a chemical deposition method. The physicochemical of Ag-doped $Bi_2WO_6/Bi_{14}W_2O_{27}$ composite film were characterized by X-ray Diffraction (XRD), Raman Spectroscopy, Scanning Electron Microscopy-Energy Dispersive Spectroscopy (SEM-EDS), X-ray Photoelectron Spectroscopy (XPS), UV-vis Spectroscopy and Photoluminescence (PL) techniques. The photocatalytic activity was studied using RhB as organic compounds at the concentration of 0.125×10^{-5} mol/L under visible light irradiation for 7 hours.

8.1 Physical appearance

The films were prepared by a chemical deposition method on glass slide substrate. Figure 8.1 shows pure Bi_2WO_6, 0.2% Ag-doped $Bi_2WO_6/Bi_{14}W_2O_{27}$, 0.5% Ag-doped $Bi_2WO_6/Bi_{14}W_2O_{27}$, 1.0% Ag-doped $Bi_2WO_6/Bi_{14}W_2O_{27}$, 3.0% Ag-doped $Bi_2WO_6/Bi_{14}W_2O_{27}$, 5.0% Ag-doped $Bi_2WO_6/Bi_{14}W_2O_{27}$, 6.0% Ag-doped $Bi_2WO_6/Bi_{14}W_2O_{27}$ and 10.0% Ag-doped $Bi_2WO_6/Bi_{14}W_2O_{27}$ composite films. The Bi_2WO_6 film displays a white color. The Ag-doped $Bi_2WO_6/Bi_{14}W_2O_{27}$ composite films were changed the color to yellow and purple with increasing the mole of silver ion (Ag^+).

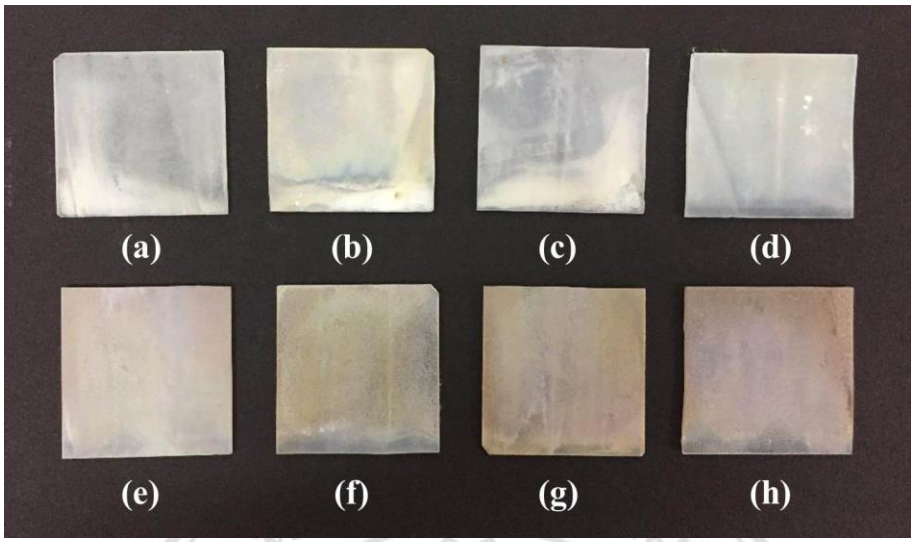

Figure 8.1 The physical appearance of (a) pure Bi_2WO_6, (b) 0.2% Ag-doped $Bi_2WO_6/Bi_{14}W_2O_{27}$, (c) 0.5% Ag-doped $Bi_2WO_6/Bi_{14}W_2O_{27}$, (d) 1.0% Ag-doped $Bi_2WO_6/Bi_{14}W_2O_{27}$, (e) 3.0% Ag-doped $Bi_2WO_6/Bi_{14}W_2O_{27}$, (f) 5.0% Ag-doped $Bi_2WO_6/Bi_{14}W_2O_{27}$, (g) 6.0% Ag-doped $Bi_2WO_6/Bi_{14}W_2O_{27}$ and (h) 10.0% Ag-doped $Bi_2WO_6/Bi_{14}W_2O_{27}$ composite films.

8.2 X-ray Diffraction (XRD)

Figure 8.2 and 8.3 show XRD patterns of all films for unwashed and washed film by DI water, respectively. The diffraction peaks at 2θ of 28.28°, 32.78°, 47.08° and 55.82° that correspond to the orthorhombic structure of pure Bi_2WO_6 (JCPDS no. 39-0256). The peaks were indexed to the (131), (200), (202) and (331) planes, respectively. The Ag-doped $Bi_2WO_6/Bi_{14}W_2O_{27}$ composite films exhibit the Bi_2WO_6 and $Bi_{14}W_2O_{27}$ phases. The $Bi_{14}W_2O_{27}$ peaks at 2θ of 27.51°, 31.96°, 45.76° and 54.28°, which can be conformed to (312), (420), (424) and (552) planes, respectively. The diffraction pattern of $Bi_{14}W_2O_{27}$ shows tetragonal structure (JCPDS no. 39-0061). The $Bi_{14}W_2O_{27}$ phase can be observed in the XRD patterns when the 0.2%, 1.0%, 3.0%, 5.0%, 6.0% and 10.0% of Ag were doped into the reaction system (Figure 8.2) [1]. The Ag-doped $Bi_2WO_6/Bi_{14}W_2O_{27}$ composite films (0.5%Ag-doped $Bi_2WO_6/Bi_{14}W_2O_{27}$, 1.0%Ag-doped $Bi_2WO_6/Bi_{14}W_2O_{27}$, 3.0%Ag-doped $Bi_2WO_6/Bi_{14}W_2O_{27}$, 5.0%Ag-doped $Bi_2WO_6/Bi_{14}W_2O_{27}$ and 10.0%Ag-doped $Bi_2WO_6/Bi_{14}W_2O_{27}$ composite films) exhibit the impurity peaks at about 37° and 43°. Nevertheless, the 5.0%Ag-doped $Bi_2WO_6/Bi_{14}W_2O_{27}$ composite film does not show the impurity after washing by DI

water (Figure 8.3). The crystallite size of Bi_2WO_6 can be calculated using the Scherrer's equation at the plane of (131). The unwashed pure Bi_2WO_6, 0.2% Ag-doped $Bi_2WO_6/Bi_{14}W_2O_{27}$, 0.5% Ag-doped $Bi_2WO_6/Bi_{14}W_2O_{27}$, 1.0% Ag-doped $Bi_2WO_6/Bi_{14}W_2O_{27}$, 3.0% Ag-doped $Bi_2WO_6/Bi_{14}W_2O_{27}$, 5.0% Ag-doped $Bi_2WO_6/Bi_{14}W_2O_{27}$, 6.0% Ag-doped $Bi_2WO_6/Bi_{14}W_2O_{27}$ and 10.0% Ag-doped $Bi_2WO_6/Bi_{14}W_2O_{27}$ composite films were calculated to be 26.49, 26.37, 30.47, 24.22, 29.88, 34.96, 24.27 and 35.38 nm, respectively. The washed pure Bi_2WO_6, 0.2% Ag-doped $Bi_2WO_6/Bi_{14}W_2O_{27}$, 0.5% Ag-doped $Bi_2WO_6/Bi_{14}W_2O_{27}$, 1.0% Ag-doped $Bi_2WO_6/Bi_{14}W_2O_{27}$, 3.0% Ag-doped $Bi_2WO_6/Bi_{14}W_2O_{27}$, 5.0% Ag-doped $Bi_2WO_6/Bi_{14}W_2O_{27}$, 6.0% Ag-doped $Bi_2WO_6/Bi_{14}W_2O_{27}$ and 10.0% Ag-doped $Bi_2WO_6/Bi_{14}W_2O_{27}$ composite films were calculated to be 29.29, 25.30, 25.62, 26.20, 23.67, 30.12, 40.75 and 29.13 nm, respectively.

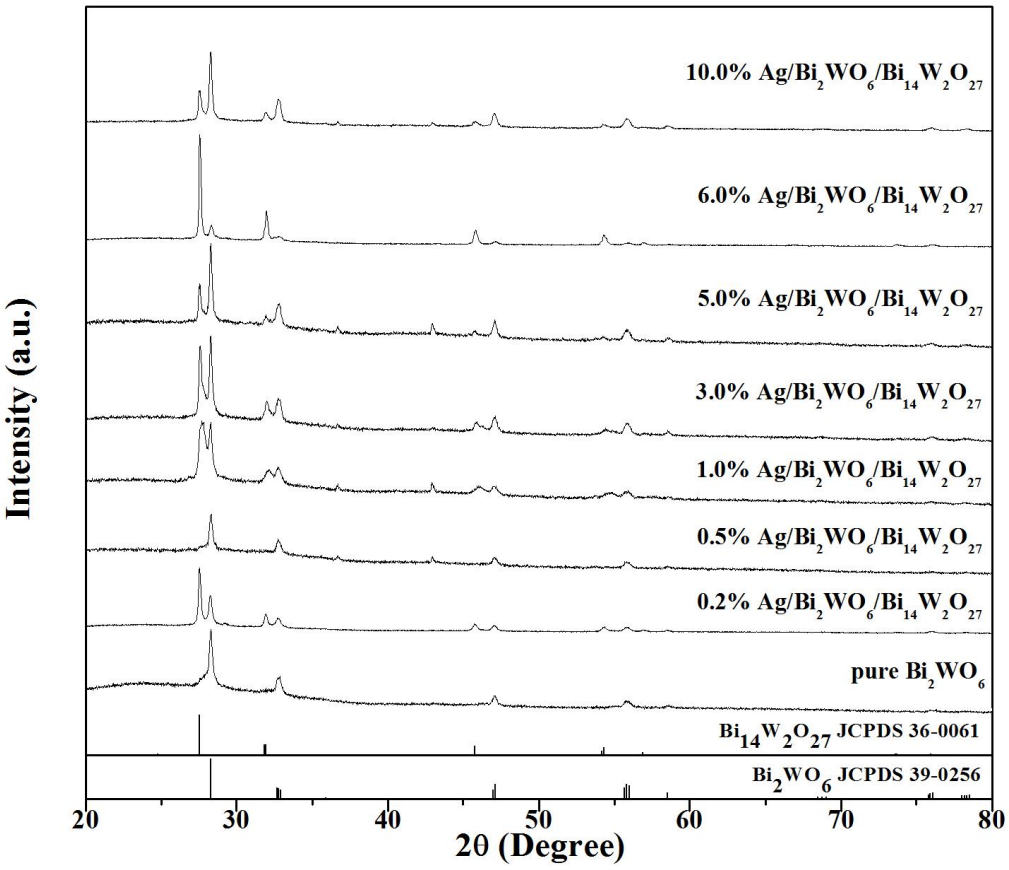

Figure 8.2 XRD patterns of all unwashed films.

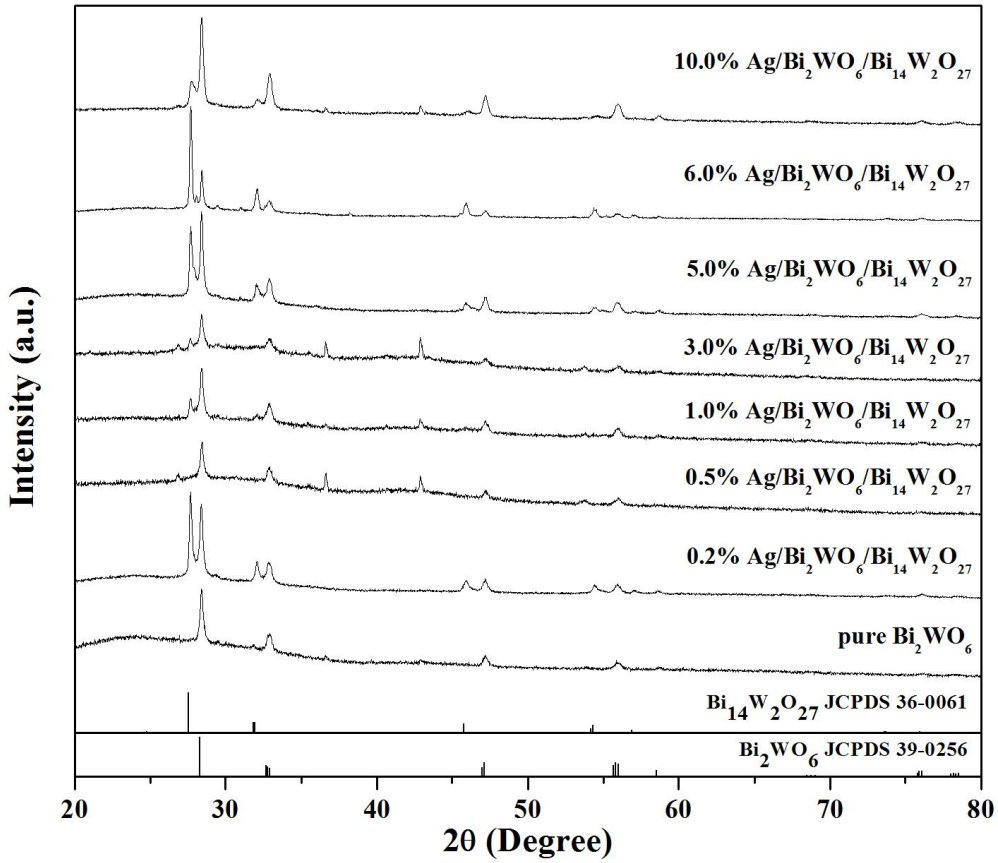

Figure 8.3 XRD patterns of all washed films.

8.3 Raman spectroscopy

Raman spectroscopy confirms the formation crystal phase of semiconductors. The Raman spectra of the pure Bi_2WO_6 and 5.0%Ag-doped $Bi_2WO_6/Bi_{14}W_2O_{27}$ composite films are presented in Figure 8.4. The Raman shifts of pure Bi_2WO_6 are located at about 152.58, 207.01, 261.24, 283.69, 307.11, 330.72, 418.76, 709.73, 789.65 and 824.67 cm^{-1}, which can be implied to the orthorhombic structure. The band at 152.58 cm^{-1} is ascribed to the lattice modes of the bismuth and tungsten (Bi–W). The bending of WO_6 octahedra is at the peaks of 207.01, 261.24, 283.69, 307.11, 418.76 cm^{-1}. The spectrum at 330.72 cm^{-1} is attributed to the Bi–O polyhedra. The antisymmetric stretching modes of WO_6 octahedra with the vibrations of the equatorial oxygen atom within layers are at the peak of 709.73 cm^{-1}. The symmetric and antisymmetric stretching modes of terminal O–W–O groups are located at the Raman shift of 789.65 and 824.67 cm^{-1}, respectively [2]. For the 5.0%Ag-doped $Bi_2WO_6/Bi_{14}W_2O_{27}$ composite film, the Raman

peaks are similar to the pure Bi_2WO_6 peaks but it has the additional peaks at 551.39, 889.12, 924.36 and 1094.30 cm^{-1}. The Raman spectra of Ag–O vibrations are appeared at 551.39, 889.12, 924.36 and 1094.30 cm^{-1} [3].

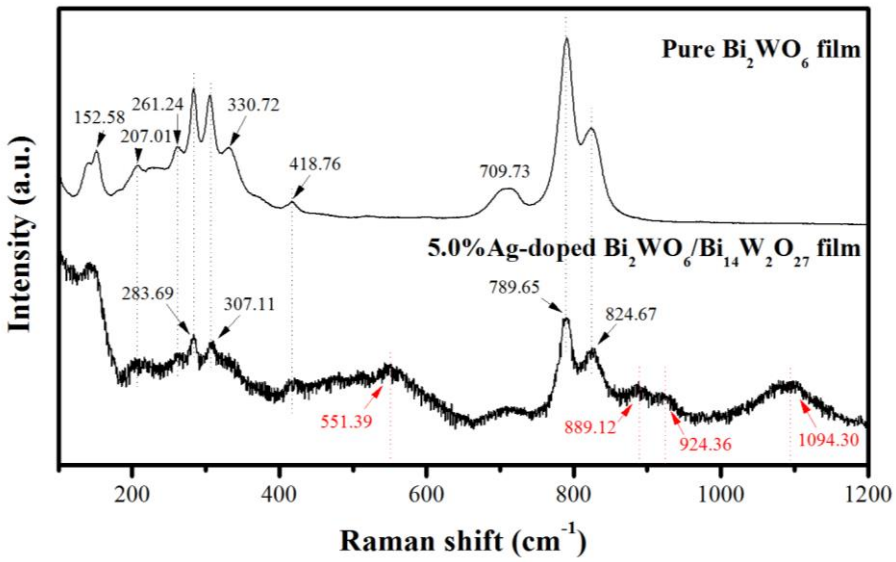

Figure 8.4 Raman spectra of pure Bi_2WO_6 and 5.0%Ag-doped $Bi_2WO_6/Bi_{14}W_2O_{27}$ composite films.

8.4 Scanning Electron Microscopy-Energy Dispersive Spectroscopy (SEM-EDS)

The morphology and cross-section of pure Bi_2WO_6 and 5.0%Ag-doped $Bi_2WO_6/Bi_{14}W_2O_{27}$ composite films were characterized by SEM, as exhibited in Figure 8.5 and 8.6. The morphology of pure Bi_2WO_6 film shows the sphere-like shape with the diameter of 100-600 nm for unwashed Bi_2WO_6 (Figure 8.5a) and the diameter of 100-300 nm for washed Bi_2WO_6 (Figure 8.5b). The 5.0%Ag-doped $Bi_2WO_6/Bi_{14}W_2O_{27}$ composite film displays the morphology of the sphere-like shape with the diameter of 100-400 nm for unwashed 5.0%Ag-doped $Bi_2WO_6/Bi_{14}W_2O_{27}$ composite film (Figure 8.5c) and the diameter of 100-200 nm for washed 5.0%Ag-doped $Bi_2WO_6/Bi_{14}W_2O_{27}$ composite film (Figure 8.5d). However, the particles of 5.0%Ag-doped $Bi_2WO_6/Bi_{14}W_2O_{27}$ composite film were agglomerated more than pure Bi_2WO_6 film. Figure 8.6 shows the cross-section of pure Bi_2WO_6 and 5.0%Ag-doped $Bi_2WO_6/Bi_{14}W_2O_{27}$ composite films. The thickness of unwashed Bi_2WO_6, washed Bi_2WO_6, unwashed 5.0%Ag-doped $Bi_2WO_6/Bi_{14}W_2O_{27}$ and washed 5.0%Ag-doped

$Bi_2WO_6/Bi_{14}W_2O_{27}$ composite films were measured to be 0.454, 0.489, 0.455 and 0.250 μm, respectively. The average thicknesses of unwashed Bi_2WO_6, washed Bi_2WO_6, unwashed 5.0%Ag-doped $Bi_2WO_6/Bi_{14}W_2O_{27}$ and washed 5.0%Ag-doped $Bi_2WO_6/Bi_{14}W_2O_{27}$ composite films were found to be 0.49±0.03, 0.50±0.04, 0.45±0.01 and 0.27±0.03 μm, as shown in Figure 8.7. The compositions of 5.0%Ag-doped $Bi_2WO_6/Bi_{14}W_2O_{27}$ composite film were investigated using EDS mapping technique. Figure 8.8 displays the EDS mapping of washed 5.0%Ag-doped $Bi_2WO_6/Bi_{14}W_2O_{27}$ composite film. The elements of 5.0%Ag-doped $Bi_2WO_6/Bi_{14}W_2O_{27}$ composite film are shown in Figure 8.9. The elements of unwashed 5.0%Ag-doped $Bi_2WO_6/Bi_{14}W_2O_{27}$ composite film was found to be 28.14%, 8.67%, 61.57% and 1.62% for Bi, W, O and Ag, respectively (Figure 8.9a). The Bi, W, O and Ag elements of washed 5.0%Ag-doped $Bi_2WO_6/Bi_{14}W_2O_{27}$ composite film was found to be 26.44%, 9.92%, 62.94% and 0.70%, respectively (Figure 8.9b). It can be observed that the Ag element decreased after washing the 5.0%Ag-doped $Bi_2WO_6/Bi_{14}W_2O_{27}$ composite film.

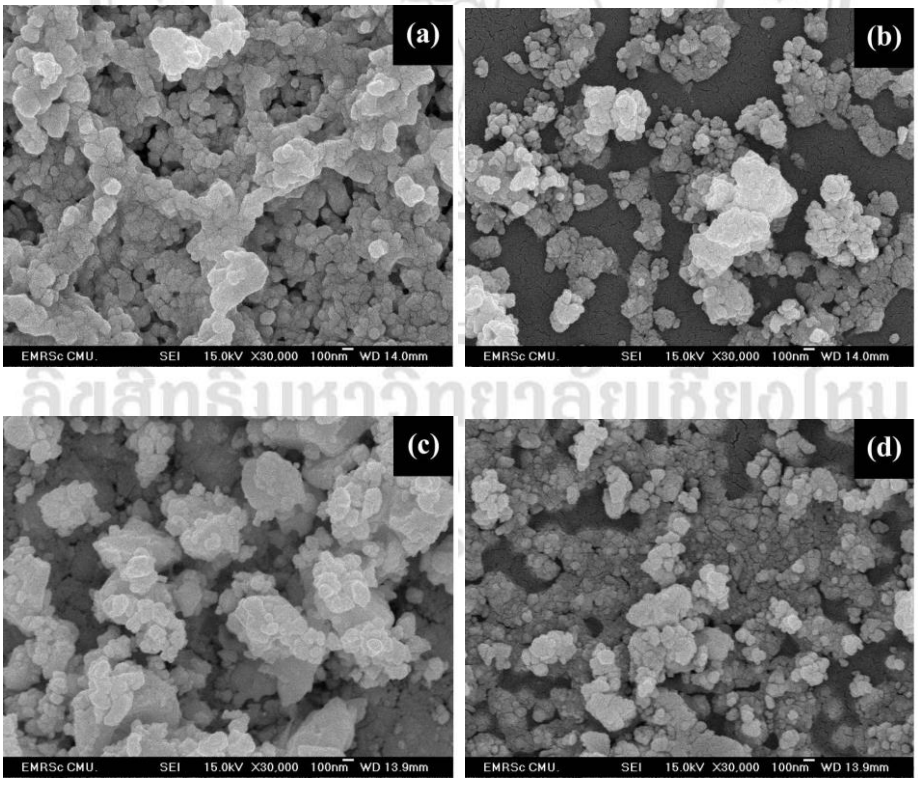

Figure 8.5 SEM images of (a) unwashed Bi_2WO_6, (b) washed Bi_2WO_6, (c) unwashed 5.0%Ag-doped $Bi_2WO_6/Bi_{14}W_2O_{27}$ and (d) washed 5.0%Ag-doped $Bi_2WO_6/Bi_{14}W_2O_{27}$ composite films.

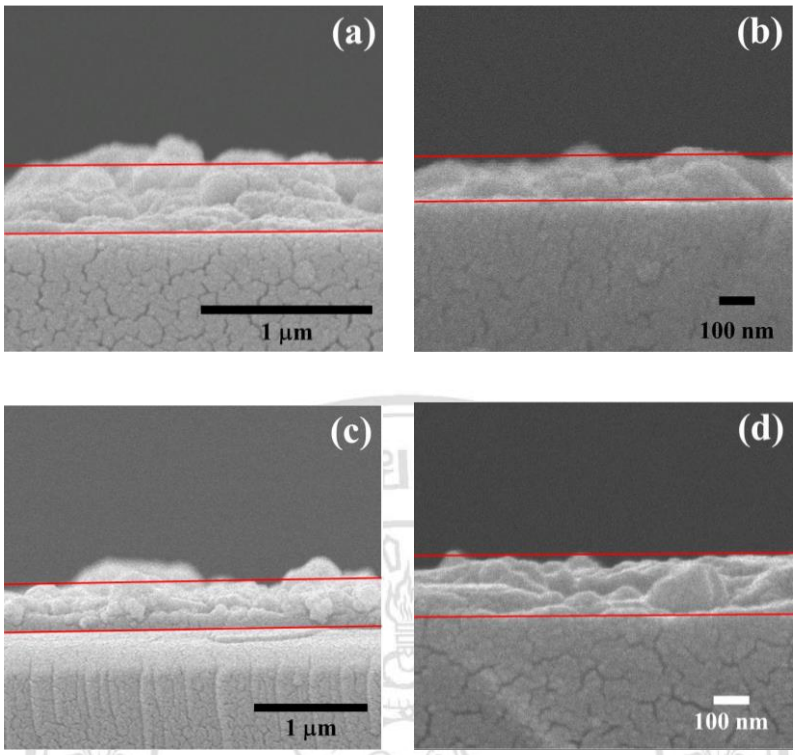

Figure 8.6 Cross-section images of (a) unwashed Bi_2WO_6, (b) washed Bi_2WO_6, (c) unwashed 5.0%Ag-doped $Bi_2WO_6/Bi_{14}W_2O_{27}$ and (d) washed 5.0%Ag-doped $Bi_2WO_6/Bi_{14}W_2O_{27}$ composite films.

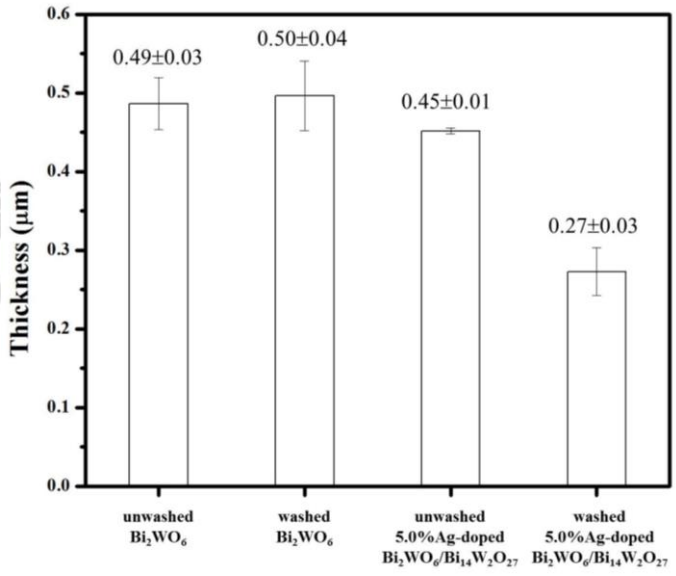

Figure 8.7 Average thickness of unwashed Bi_2WO_6, washed Bi_2WO_6, unwashed 5.0%Ag-doped $Bi_2WO_6/Bi_{14}W_2O_{27}$ and washed 5.0%Ag-doped $Bi_2WO_6/Bi_{14}W_2O_{27}$ composite films.

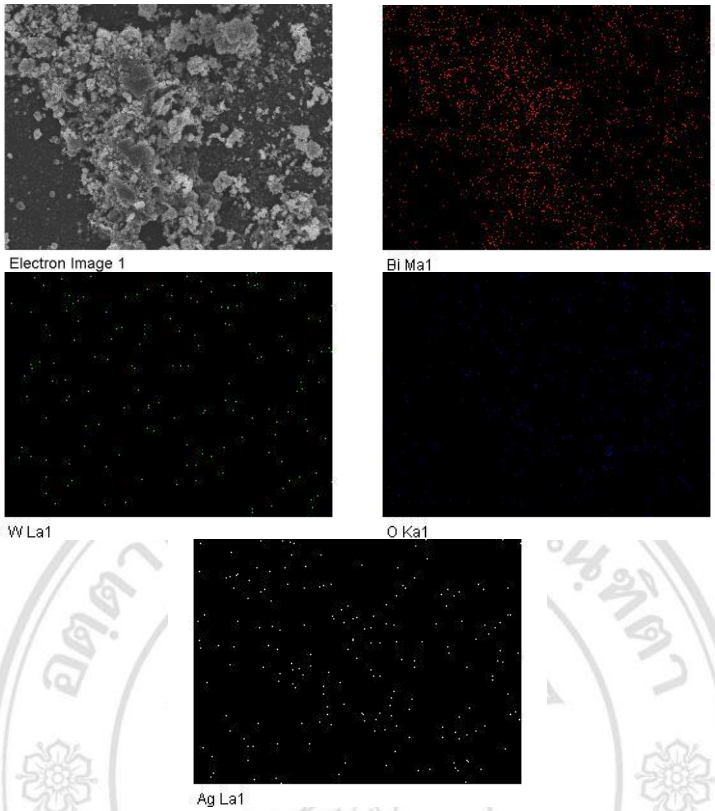

Figure 8.8 EDS mapping of Bi, W, O and Ag elements in washed 5.0%Ag-doped $Bi_2WO_6/Bi_{14}W_2O_{27}$ composite film.

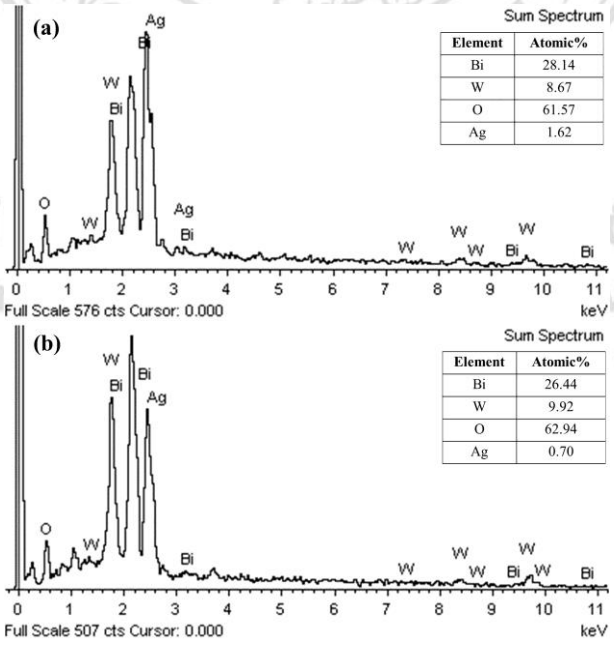

Figure 8.9 The compositions of (a) unwashed 5.0%Ag-doped $Bi_2WO_6/Bi_{14}W_2O_{27}$ and (b) washed 5.0%Ag-doped $Bi_2WO_6/Bi_{14}W_2O_{27}$ composite films.

8.5 X-Ray Photoelectron Spectroscopy (XPS)

XPS analysis was investigated to confirm the compositions and valence states of Bi, W, Ag and O for pure Bi_2WO_6 and 5.0%Ag-doped $Bi_2WO_6/Bi_{14}W_2O_{27}$ composite films. Figure 8.10a shows the binding energy of Bi 4f. The binding energy peaks at about 164.00 and 159.00 eV are ascribed to the Bi $4f_{5/2}$ and Bi $4f_{7/2}$, respectively, which can be indicated to Bi^{3+} in Bi_2WO_6. However, the higher shifted peaks at about 166.00, 165.00 and 160.00 eV are referred to the oxidation state of Bi^{4+} or Bi^{5+} [4]. The main binding energy peaks of W $4f_{5/2}$ and W $4f_{7/2}$ located at 37.16 and 35.06 eV, respectively, corresponding to W^{6+} in Bi_2WO_6 (Figure 8.10b). The XPS peaks of 5.0%Ag-doped $Bi_2WO_6/Bi_{14}W_2O_{27}$ composite film placed at 37.53, 36.77, 35.43 and 34.65 eV. The two shifted peaks at 37.53 and 35.43 eV are attributed to the oxidation state at W^{5+} [5]. The shifted binding energy of 5.0%Ag-doped $Bi_2WO_6/Bi_{14}W_2O_{27}$ composite film compared with pure Bi_2WO_6, corresponding to the bonds in composite. The O 1s spectra of pure Bi_2WO_6 and 5.0%Ag-doped $Bi_2WO_6/Bi_{14}W_2O_{27}$ composite films are shown in Figure 8.10c. The peak of O1s at 529.62 and 529.87 eV are implied to the lattice oxygen in the metal oxide. The chemisorbed oxygen or weakly bond oxygen species located at the peak of 530.94 and 530.99 eV. The XPS peaks at 532.14, 532.45 and 533.64 eV are ascribed to the surface oxygen by hydroxyl species or adsorb water species on the surface [6]. Figure 7.9d shows the XPS spectrum of Ag ion in 5.0%Ag-doped $Bi_2WO_6/Bi_{14}W_2O_{27}$ composite film. The peaks at 367.70 eV and 373.60 eV for Ag $3d_{5/2}$ and Ag $3d_{3/2}$, respectively, can be attributed to Ag^+ [7].

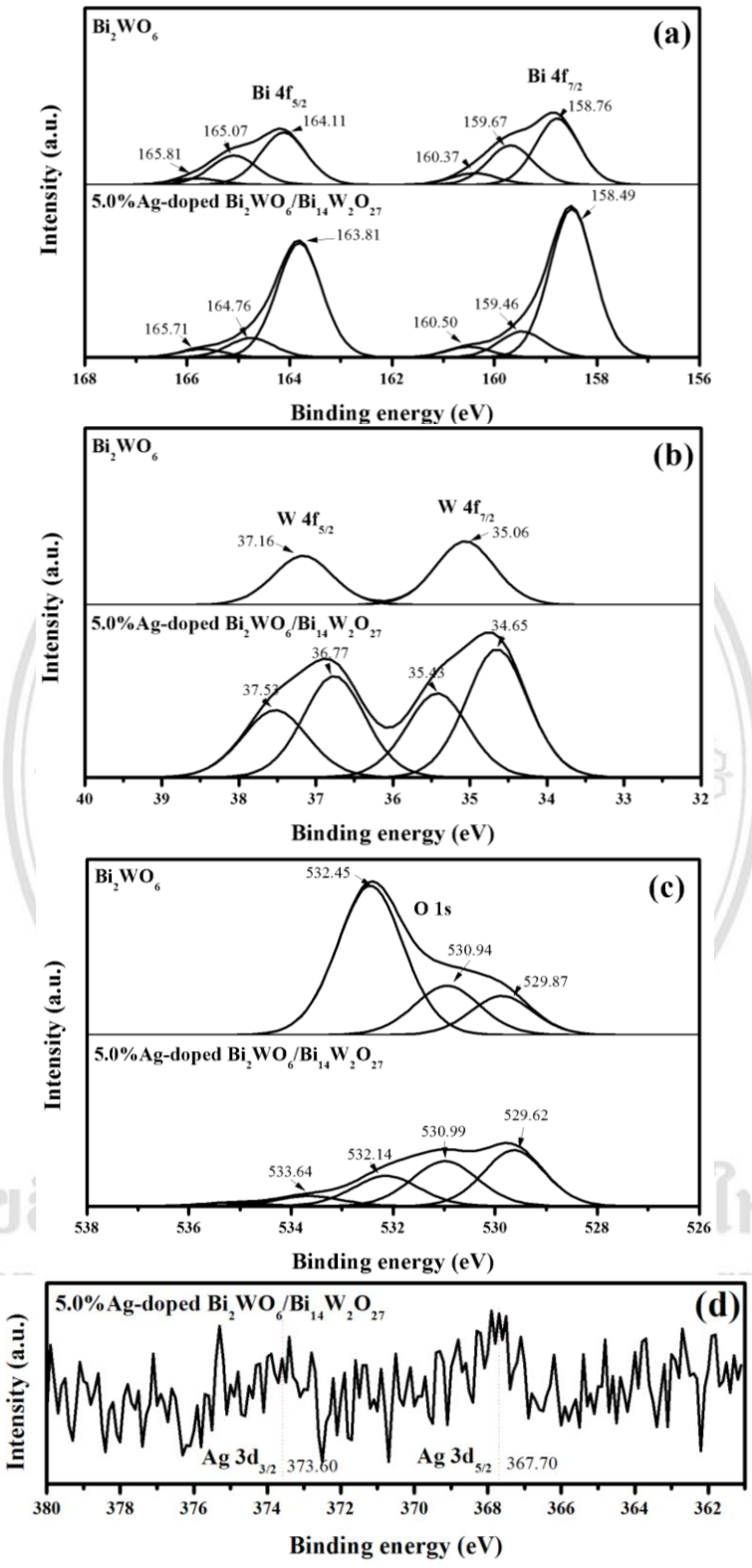

Figure 8.10 XPS spectra of (a) Bi 4f, (b) W 4f, (c) O 1s and (d) Ag 3d for pure Bi_2WO_6 and 5.0%Ag-doped $Bi_2WO_6/Bi_{14}W_2O_{27}$ composite films.

8.6 UV-vis spectroscopy

The absorbance spectra of pure Bi_2WO_6 and 5.0%Ag-doped $Bi_2WO_6/Bi_{14}W_2O_{27}$ composite films were examined using UV-vis spectroscopy, as displayed in Figure 8.11. It can be observed that the pure Bi_2WO_6 and 5.0%Ag-doped $Bi_2WO_6/Bi_{14}W_2O_{27}$ composite films absorbed the light in visible region at 421 and 424 nm, respectively. The band gap energies were calculated as 2.95 and 2.92 eV for pure Bi_2WO_6 and 5.0%Ag-doped $Bi_2WO_6/Bi_{14}W_2O_{27}$ composite films, respectively.

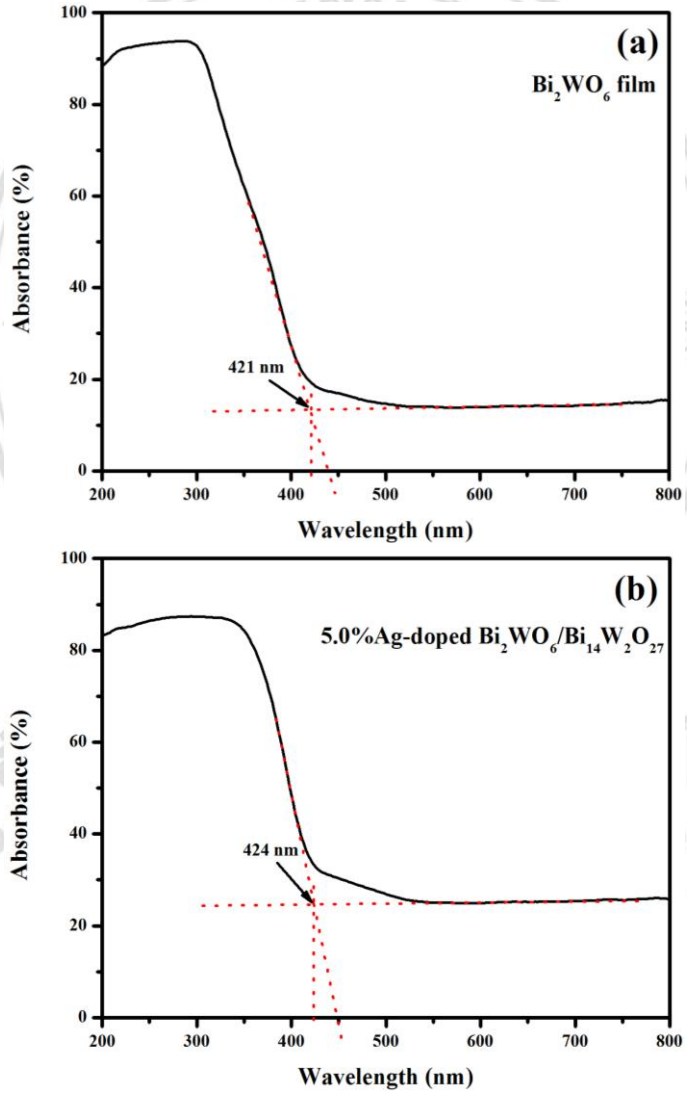

Figure 8.11 UV-vis DRS spectra of (a) pure Bi_2WO_6 and (b) 5.0%Ag-doped $Bi_2WO_6/Bi_{14}W_2O_{27}$ composite films.

8.7 Photocatalytic activity

Pure Bi_2WO_6, 0.2%Ag-doped $Bi_2WO_6/Bi_{14}W_2O_{27}$, 0.5%Ag-doped $Bi_2WO_6/Bi_{14}W_2O_{27}$, 1.0%Ag-doped $Bi_2WO_6/Bi_{14}W_2O_{27}$, 3.0%Ag-doped $Bi_2WO_6/Bi_{14}W_2O_{27}$, 5.0%Ag-doped $Bi_2WO_6/Bi_{14}W_2O_{27}$, 6.0%Ag-doped $Bi_2WO_6/Bi_{14}W_2O_{27}$ and 10.0%Ag-doped $Bi_2WO_6/Bi_{14}W_2O_{27}$ composite films were estimated the photocatalytic degradation of RhB under visible light irradiation for 7 hours. Figure 8.12 shows the photocatalytic activity trend of all films. It can be observed that the 5.0%Ag-doped $Bi_2WO_6/Bi_{14}W_2O_{27}$ composite film exhibits the highest photocatalytic efficiency (57.07%) for RhB degradation. Pseudo-first-order reaction [$-\ln (C/C_0) = kt$] was plotted to determine the reaction rate constants (k), as shown in Figure 8.13. The 5.0%Ag-doped $Bi_2WO_6/Bi_{14}W_2O_{27}$ composite film promotes high reaction rate constant of 0.1409 $hour^{-1}$. The k value of 5.0%Ag-doped $Bi_2WO_6/Bi_{14}W_2O_{27}$ composite film relates to high photocatalytic performance. The summary of the photocatalytic efficiency and reaction rate constants of all films for RhB degradation is shown in Table 8.1.

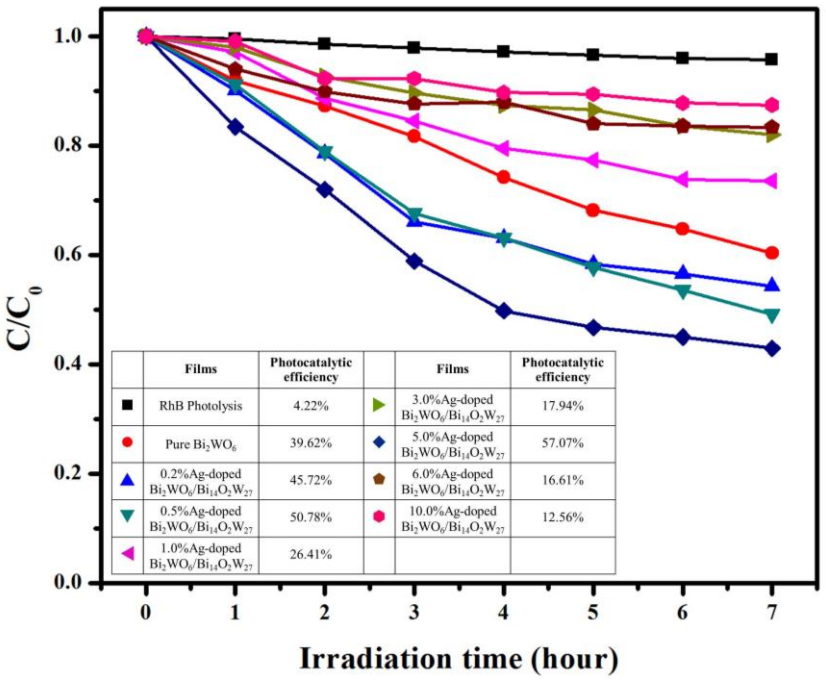

Figure 8.12 The photocatalytic activity of all films for RhB degradation.

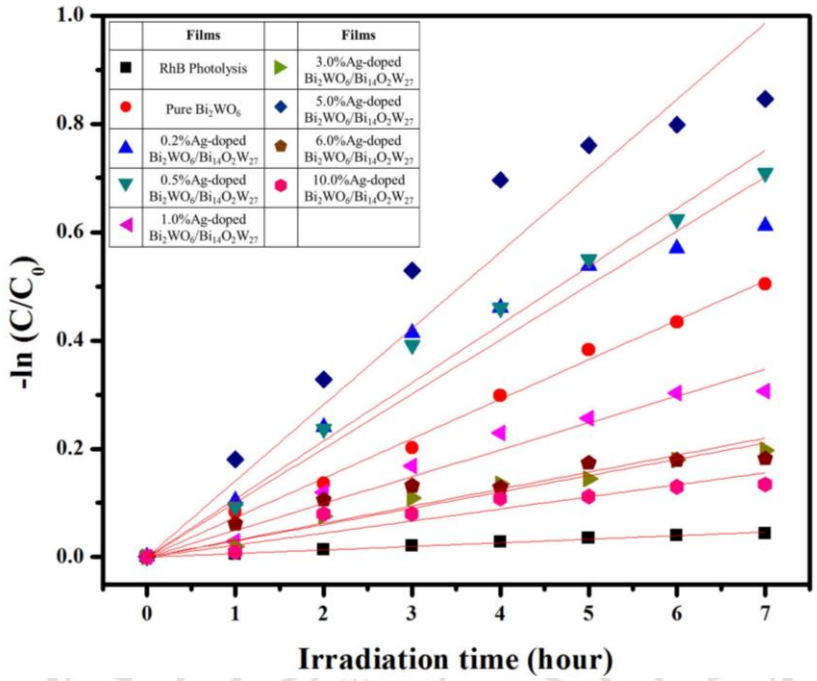

Figure 8.13 Pseudo-first-order reactions of all films for RhB degradation.

Table 8.1 The photocatalytic efficiency and reaction rate constants (k) of all films for RhB degradation.

Films	**Photocatalytic efficiency**	***k* (hour^{-1})**	***R*^{2}**
RhB Photolysis	4.22%	0.0066	0.9959
Pure Bi_2WO_6	39.62%	0.0729	0.9986
0.2%Ag/$Bi_2WO_6/Bi_{14}W_2O_{27}$	45.72%	0.1004	0.9774
0.5%Ag/$Bi_2WO_6/Bi_{14}W_2O_{27}$	50.78%	0.1074	0.9938
1.0%Ag/$Bi_2WO_6/Bi_{14}W_2O_{27}$	26.41%	0.0496	0.9871
3.0%Ag/$Bi_2WO_6/Bi_{14}W_2O_{27}$	17.94%	0.0301	0.9900
5.0%Ag/$Bi_2WO_6/Bi_{14}W_2O_{27}$	57.07%	0.1409	0.9767
6.0%Ag/$Bi_2WO_6/Bi_{14}W_2O_{27}$	16.61%	0.0314	0.9525
10.0%Ag/$Bi_2WO_6/Bi_{14}W_2O_{27}$	12.56%	0.0223	0.9615

8.8 Photocatalytic stability

The photocatalytic stability of 5.0%Ag-doped $Bi_2WO_6/Bi_{14}W_2O_{27}$ composite film was examined by the recyclability of the film for 10 times. Figure 8.14 shows the photocatalytic performance of the 5.0%Ag-doped $Bi_2WO_6/Bi_{14}W_2O_{27}$ composite film. It can be seen that the photo stability of 5.0%Ag-doped $Bi_2WO_6/Bi_{14}W_2O_{27}$ composite film exhibits the efficiency of 57.07%, 56.56%, 50.89%, 50.85%, 47.34%, 46.18%, 45.13%, 41.13%, 38.33% and 36.21% for tenth times. The photocatalytic activity was gradually decreased after tenth cycle. It confirms that the 5.0%Ag-doped $Bi_2WO_6/Bi_{14}W_2O_{27}$ composite film has the good photocatalytic stability.

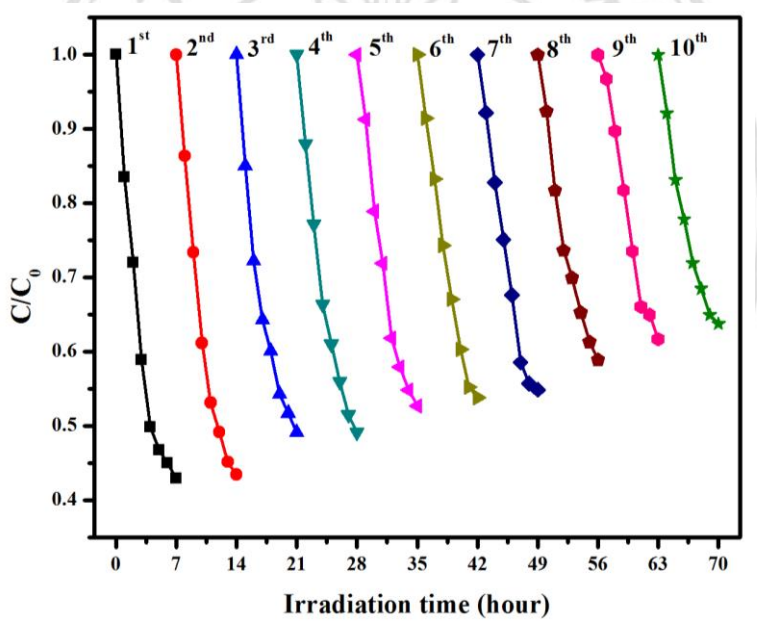

Figure 8.14 The photocatalytic stability of the 5.0%Ag-doped $Bi_2WO_6/Bi_{14}W_2O_{27}$ composite film.

8.9 Active species trapping

The active species of the 5.0%Ag-doped $Bi_2WO_6/Bi_{14}W_2O_{27}$ composite film during the photocatalytic reaction was detected by adding 1×10^{-9} mol/L of 2-isopropanol (IPA) (a quencher of $\cdot OH$), p-benzoquinone (BQ) (a quencher of $\cdot O_2^-$), and potassium iodide (KI) (a quencher of h^+). It can be observed that the photocatalytic activity for RhB degradation decreased when filling the quenchers, as seen in Figure 8.15. The photocatalytic performance of the 5.0%Ag-doped $Bi_2WO_6/Bi_{14}W_2O_{27}$

composite film for RhB degradation under visible light irradiation is slightly decreased after adding IPA (2.85%). The photocatalytic efficiency of the 5.0%Ag-doped $Bi_2WO_6/Bi_{14}W_2O_{27}$ composite film after adding IPA is lower than BQ (18.03%) and KI (18.34%). It can be concluded that the *·OH* radicals are the main active specie during the photocatalytic reaction of the 5.0%Ag-doped $Bi_2WO_6/Bi_{14}W_2O_{27}$ composite film for RhB degradation.

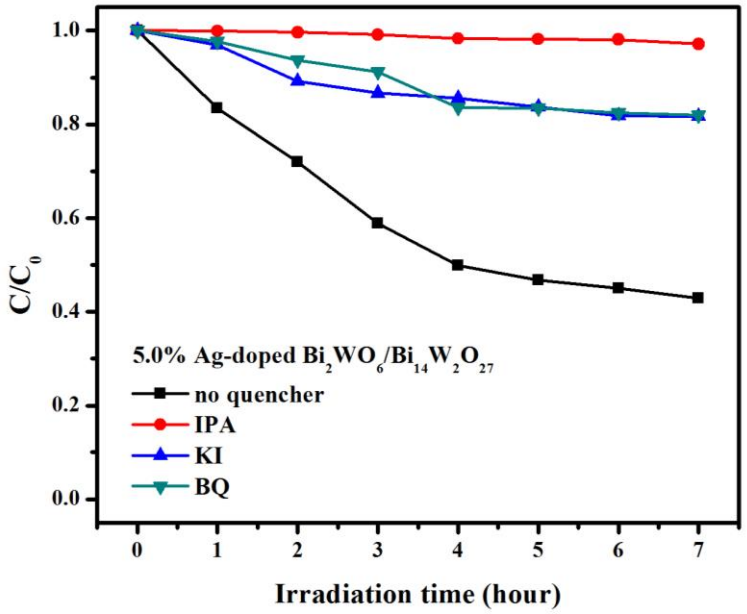

Figure 8.15 The active species trapping of the 5.0%Ag-doped $Bi_2WO_6/Bi_{14}W_2O_{27}$ composite film for RhB degradation using IPA, KI and BQ.

8.10 Photoluminescence (PL)

Photoluminescence technique was considered to apply for detecting the electron-hole recombination of the semiconductor. Figure 8.16 shows the PL peaks of pure Bi_2WO_6 and 5.0%Ag-doped $Bi_2WO_6/Bi_{14}W_2O_{27}$ composite films. It can be observed that the emission peaks are located at 482.85 and 483.40 nm for of pure Bi_2WO_6 and 5.0%Ag-doped $Bi_2WO_6/Bi_{14}W_2O_{27}$ composite films, respectively. As the result, the PL intensity of the 5.0%Ag-doped $Bi_2WO_6/Bi_{14}W_2O_{27}$ composite film is lower than pure Bi_2WO_6 film, which infers that the 5.0%Ag-doped $Bi_2WO_6/Bi_{14}W_2O_{27}$ composite film has low the recombination rate of the photogenerated electron-hole pairs in the photocatalytic reaction. Accordingly, the 5.0%Ag-doped $Bi_2WO_6/Bi_{14}W_2O_{27}$ composite

film exhibits the highest photocatalytic performance, compared with pure Bi_2WO_6 and other films. This demonstrated that the 5.0%Ag-doped $Bi_2WO_6/Bi_{14}W_2O_{27}$ composite film can be reduced the electron-hole pairs recombination.

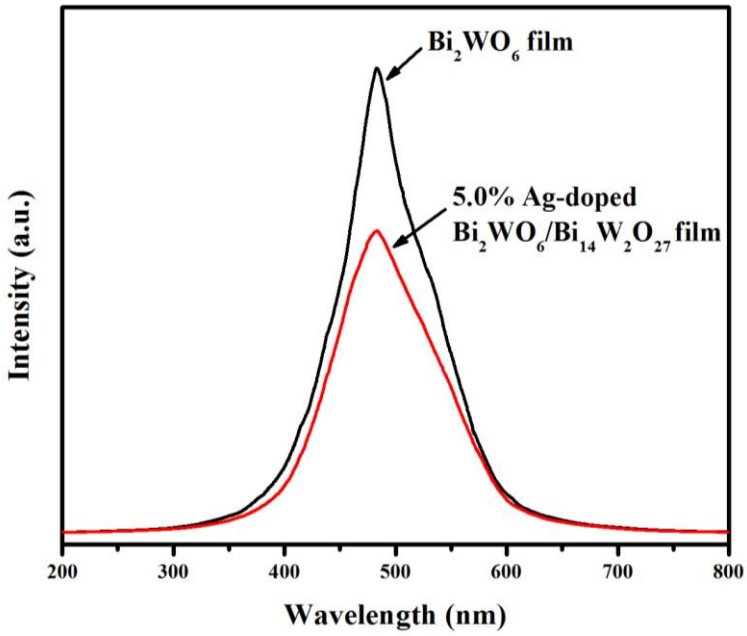

Figure 8.16 PL spectra of pure Bi_2WO_6 and 5.0%Ag-doped $Bi_2WO_6/Bi_{14}W_2O_{27}$ composite films.

8.11 The photocatalytic mechanism of Ag-doped $Bi_2WO_6/Bi_{14}W_2O_{27}$ composite film

Figure 8.16 shows the possible photocatalytic mechanism of Ag-doped $Bi_2WO_6/Bi_{14}W_2O_{27}$ composite film for RhB degradation under visible light irradiation. In the photocatalytic process, the Ag-doped $Bi_2WO_6/Bi_{14}W_2O_{27}$ composite film absorbed the light in the visible region. The electrons are stimulated and migrated from valence band to conduction band, resulting electron-hole pairs. The electrons and holes can be transferred between Bi_2WO_6 and $Bi_{14}W_2O_{27}$ at the surface. The holes generated $\cdot OH$ by the oxidation reaction with H_2O or OH^-. In order to reach the high photocatalytic performance, the Ag group was added into the $Bi_2WO_6/Bi_{14}W_2O_{27}$ composite film [8]. The Ag^+ ion can trap electrons, which produced $\cdot O_2^-$ using reduction reaction with O_2.

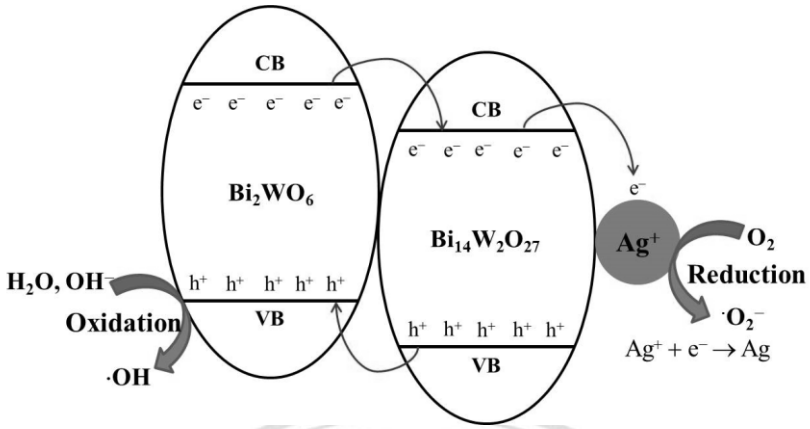

Figure 8.17 Photocatalytic mechanism of Ag-doped $Bi_2WO_6/Bi_{14}W_2O_{27}$ composite film for RhB degradation.

8.12 Conclusions

The Ag-doped $Bi_2WO_6/Bi_{14}W_2O_{27}$ composite film was successfully synthesized by a chemical deposition method. The XRD pattern of the Ag-doped $Bi_2WO_6/Bi_{14}W_2O_{27}$ composite film shows the both structures of orthorhombic Bi_2WO_6 and tetragonal $Bi_{14}W_2O_{27}$. The crystallite size of the 5.0%Ag-doped $Bi_2WO_6/Bi_{14}W_2O_{27}$ composite film is biggest (34.96 nm). The Raman peak is confirmed that the 5.0%Ag-doped $Bi_2WO_6/Bi_{14}W_2O_{27}$ composite film have the orthorhombic phase of Bi_2WO_6. The morphology of Bi_2WO_6 and Ag-doped $Bi_2WO_6/Bi_{14}W_2O_{27}$ composite films is the sphere-like shape. The EDS analysis was confirmed that the 5.0%Ag-doped $Bi_2WO_6/Bi_{14}W_2O_{27}$ composite film consists of Bi, W, O and Ag elements. The thickness of Bi_2WO_6 film is thicker than 5.0%Ag-doped $Bi_2WO_6/Bi_{14}W_2O_{27}$ composite film. The chemical composition and chemical state were ensured by XPS analysis. The 5.0%Ag-doped $Bi_2WO_6/Bi_{14}W_2O_{27}$ composite film includes Bi^{3+}, Bi^{4+}, Bi^{5+}, W^{5+}, O^{2-} and Ag^{+} compositions. The Bi_2WO_6 and 5.0%Ag-doped $Bi_2WO_6/Bi_{14}W_2O_{27}$ composite films can be responded in visible light region with the band gap of 2.95 eV and 2.92 eV, respectively. The 5.0%Ag-doped $Bi_2WO_6/Bi_{14}W_2O_{27}$ composite film exhibits the best photocatalytic efficiency (57.07%) for RhB degradation under visible light irradiation in 7 hours. The 5.0%Ag-doped $Bi_2WO_6/Bi_{14}W_2O_{27}$ composite film shows the good photocatalytic stability that can be reused for RhB degradation in tenth times. The *·OH* radicals are the main active specie of the 5.0%Ag-doped $Bi_2WO_6/Bi_{14}W_2O_{27}$ composite

film in the photocatalytic reaction. The PL technique is verified that the 5.0%Ag-doped $Bi_2WO_6/Bi_{14}W_2O_{27}$ composite film can separate electrons and holes, which affect to enhanced photocatalytic performance.

Table 8.2 The summary of physicochemical properties and photocatalytic efficiency of Ag-doped $Bi_2WO_6/Bi_{14}W_2O_{27}$ composite film.

Properties	**Bi_2WO_6 film**	**5.0% Ag-doped $Bi_2WO_6/Bi_{14}W_2O_{27}$ film**
Structure	orthorhombic	Orthorhombic/tetragonal
Crystallite size	29.29 nm	30.12 nm (Bi_2WO_6), 24.00 nm ($Bi_{14}W_2O_{27}$)
Morphology	sphere-like	sphere-like
Thickness	0.132±0.010 μm	0.187±0.007 μm
Band gap	2.95 eV	2.92 eV
Photocatalytic performance (RhB)	39.62%	57.07%
Main active specie	-	*·OH*

8.13 References

[1] Xu, X. Ge, Y. Wang, H. Li, B. Yu, L. Liang, Y. Chen, K. and Wang, F., "Sol-gel synthesis and enhanced photocatalytic activity of doped bismuth tungsten oxide composite," Materials Research Bulletin, Vol. 73, January, 2016, pp. 385-393.

[2] Huang, H. Chen, H. Xia, Y. Tao, X. Gan, Y. Weng, X. and Zhang, W., "Controllable synthesis and visible-light-responsive photocatalytic activity of Bi_2WO_6 fluffy microsphere with hierarchical architecture," Journal of Colloid and Interface Science, Vol. 370, No. 1, March 15, 2012, pp. 132-138.

[3] Natkaeo, A. Phokharatkul, D. Hodak, J. H. Wisitsoraat and A. Hodak, S. K., "Highly selective sub-10 ppm H_2S gas sensors based on Ag-doped $CaCu_3Ti_4O_{12}$ films," Sensors and Actuators B: Chemical, Vol. 260, May 1, 2018, pp. 571-580.

[4] Ding, X. Zhao, K. and Zhang, L., "Enhanced photocatalytic removal of sodium pentachlorophenate with self-doped Bi_2WO_6 under visible light by generating more superoxide ions," Environmental Science and Technology, Vol. 48, April 30, 2014, pp. 5823-5831.

[5] Nie, Z. P. Ma, D. K. Fang, G. Y. Chen, W. and Huang, S. M., "Concave Bi_2WO_6 nanoplates with oxygen vacancies achieving enhanced electrocatalytic oxygen evolution in near-neutral water," Journal of Materials Chemistry A, Vol. 4, 2016, pp. 2438-2444.

[6] Yang, Z. Lv, J. Pang, H. Yan, W. Qian, K. Guo, T. and Guo, Z., "Facile synthesis of coaxial CNTs/MnO_x-carbon hybrid nanofibers and their greatly enhanced lithium storage performance," Scientific Reports, Vol. 5, December 1, 2015, pp. 1-10.

[7] Yin, L. Wang, Z. Lu, L. Wan, X. and Shi, H., "Universal degradation performance of a high-efficiency AgBr/Ag_2CO_3 photocatalyst under visible light and an insight into the reaction mechanism," New Journal of Chemistry, Vol. 39, April 9, 2015, pp. 4891-4900.

[8] Dinesh, V. P. Biji, P. Ashok, A. Dhara, S. K. Kamruddin, M. Tyagi, A. K. and Rag, B., "Plasmon-mediated, highly enhanced photocatalytic degradation of industrial textile dyes using hybrid ZnO@Ag core-shell nanorods," RSC Advances, Vol. 4, October 20, 2014, pp. 58930-58940.